

Flow around an impulsively arrested circular cylinder

G. J. Sheard

Fluids Laboratory for Aeronautical and Industrial Research (FLAIR), Department of Mechanical Engineering and Monash University Biomedical Engineering Technology Alliance (MuBeta), Monash University, Victoria 3800, Australia

T. Leweke

Institut de Recherche sur les Phénomènes Hors Équilibre (IRPHÉ), UMR 6594 CNRS/Universités Aix-Marseille I & II, 49, rue Frédéric Joliot-Curie, Boite Postale 146, F-13384 Marseille Cedex 13, France

M. C. Thompson and K. Hourigan

Fluids Laboratory for Aeronautical and Industrial Research (FLAIR), Department of Mechanical Engineering and Monash University Biomedical Engineering Technology Alliance (MuBeta), Monash University, Victoria 3800, Australia

(Received 21 February 2007; accepted 22 May 2007; published online 8 August 2007)

The vortex dynamics of the flow around a suddenly arrested translating circular cylinder is investigated by direct numerical simulation and water tank experiments. In the numerical study, a method of visualization of streaklines in simulated-particle tracking computations is proposed, which is based on a variable-variance two-dimensional Gaussian-weighted summation of particles in the vicinity of each interpolation point, and for which a close similarity with physical dye visualizations is found. This technique is used to identify the trajectory of both the wake vortices, as well as the secondary vortices induced as the original wake convects over the arrested cylinder. Observations show that, in a fashion similar to the flow past an arresting sphere, each wake vortex induces a counter-rotating vortex pair, which subsequently self-propels over a range of sometimes surprising trajectories as the Reynolds number and cylinder translation distance are varied. At low Reynolds numbers and short translation distances, the wake vortices propel past the cylinder, continuing in the direction of the original cylinder motion. At higher Reynolds numbers, the vortices deviate outwards in circular arcs of increasing curvature, even to the extent that the vortex pairs collide *behind* the cylinder. These trajectory curvatures are analyzed with respect to the circulation of the vortex pairs. At sufficiently long translation distances, a wake instability destroys the reflective symmetry about the wake centerline. This regime is investigated by both comparison with experiment and analysis of the discrepancy between the vorticity and particle fields at large post-arrest times. © 2007 American Institute of Physics. [DOI: 10.1063/1.2754346]

I. INTRODUCTION

The acceleration from zero velocity of a body in a fluid, or its deceleration to rest, find widespread applications spanning vehicular aerodynamics, mixing, propulsion, ballistics, and multiphase fluid mechanics. While the case of an impulsively started flow has been studied extensively^{1,2} in relation to the motion of circular cylinders in a fluid, the case of an arresting body has received limited attention (with notable exceptions including Tatsuno and Taneda,³ Wang and Dalton⁴ for an arresting cylinder, and Leweke, Thompson, and Hourigan,⁵ and Thompson, Leweke, and Hourigan⁶ for an arresting sphere). In those studies, the flows obtained were consistent: in motion, a recirculating wake develops behind the body, comprising an attached counter-rotating vortex pair. Subsequent to arrest of the cylinder, the momentum in the surrounding fluid carries the wake back over the cylinder, and this process induces secondary vortices that pair with each wake vortex in the vicinity of the widest point around the cylinder. The trajectories of these vortices over long times have not been established to date. However, the studies did detect a variety of flow patterns depending on

factors such as the speed and length of translation of the cylinder.

This study reports on a systematic investigation of the flow regimes that develop around arresting cylinders for a wide range of Reynolds numbers and translation distances. The flows are monitored for long times after the arrest, and emphasis is placed on numerically simulating popular experimental dye visualization approaches. The apparent structure of a flow depicted by these visualization techniques is compared with the vorticity fields, and the vortex kinematics and dynamics over long times is analyzed.

Problem formulation

The problem under investigation is shown diagrammatically in Fig. 1. A circular cylinder with diameter D is initially at rest in a quiescent fluid. An impulsive translation at a constant speed U is initiated at time $t=0$. After traveling a distance L/D , the cylinder is abruptly brought to rest at time t_{arrest} . The time since arrest is $t^* = t - t_{\text{arrest}}$, where times are nondimensionalized by D/U (the time taken for the cylinder to translate one cylinder diameter). The translation distance

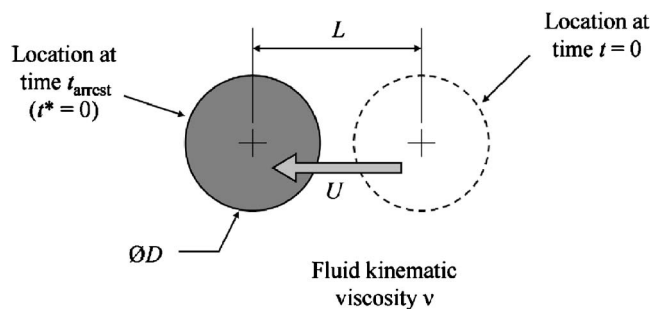


FIG. 1. The problem under investigation. The cylinder is viewed end-on, and its initial and final positions are denoted by dashed and solid circles, respectively.

L/D and the Reynolds number Re are control parameters for this problem. The Reynolds number is defined as

$$Re = \frac{UD}{\nu},$$

where ν is the kinematic viscosity of the surrounding fluid.

II. METHODOLOGY

This investigation comprises both a numerical investigation and physical dye-visualization experiments. Both are described here, though the numerical component receives greater attention as it is the primary focus of this study.

A. The spectral-element code

The numerical simulations in this investigation were conducted using a spectral-element software package *Viper*, developed within the Department of Mechanical Engineering, Monash University. Spectral element simulations are noted for their ability to compute on sparse meshes thanks to a capacity for high spatial resolution within each element through incorporation of high-order polynomials representing the flow variables, and efficient quadrature techniques for integration of the governing equations. These features enable spectral spatial convergence to be achieved.⁷ Spectral element methods have been widely used for solving laminar incompressible bluff-body flow problems (see, for example, Refs. 8–10), where the multi-element and high-order features of the method are well suited to the discretization of wake flows and flows around complex geometries.

This code permits two-dimensional calculations of time-dependent incompressible fluid flows on a mesh comprising curvilinear quadrilateral spectral elements. In a fashion similar to Thompson *et al.*⁸ and Blackburn and Sherwin,¹¹ a nodal spectral-element formulation is employed, with velocity and pressure fields being evaluated at points corresponding to the Gauss-Legendre-Lobatto quadrature points. This allows for efficient computation of the solution as the equations of motion are solved in a weak form following application of the method of weighted residuals, with the test and trial functions occupying the same polynomial space. For time integration, a third-order accurate time splitting scheme based on a backwards-multistep integration method is employed.¹²

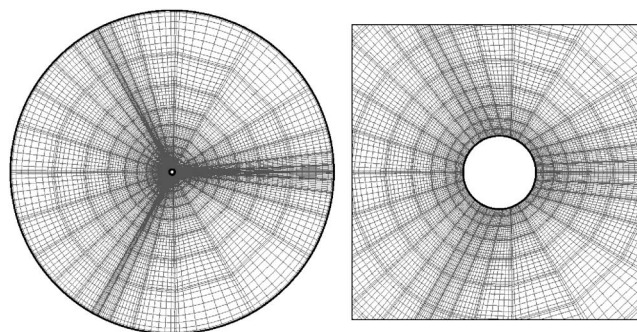


FIG. 2. The spectral-element mesh employed in this study. Shown are (left) the full mesh and (right) detail in the vicinity of the cylinder.

Computations were performed in the reference frame of the cylinder, and the arrest of the cylinder was described by simultaneously changing both the necessary boundary conditions, as well as correcting the interior velocity field for the change in velocity relative to the cylinder. Simulations are impulsively initiated from a zero velocity field, so no additional stability constraint was placed on the time integration scheme during arrest. Figure 2 shows the mesh used for this study. The mesh contained 450 spectral elements, which extended radially from the cylinder. The cylinder was surrounded by a circular computational domain with radius $30D$. On all boundaries, high-order pressure boundary conditions are imposed.¹² On the cylinder surface a zero velocity is imposed, and on the outer domain boundary, a time-dependent condition is imposed to model the arrest of the cylinder. Prior to arrest, a uniform velocity relative to the cylinder is imposed, and after arrest a zero velocity is imposed.

B. Simulated particle tracking

For visualization purposes, a numerical analogue to laser-induced fluorescent dye visualization (e.g., see Williamson¹³) was implemented using a (nearly) fourth-order time-accurate Lagrangian simulated particle tracking technique.¹⁴ With this technique, simulated particles are injected regularly into the flow in the vicinity of the cylinder, thus mimicking the entrainment of a dye from the body into the moving fluid. The new locations of these particles are calculated at regular time intervals as the simulation of the underlying flow progresses. Particle tracking is performed by updating particle positions within elements using a fourth-order Runge-Kutta time integration scheme in parametric space, while a series of linear substeps is employed to step to and across element interfaces.

A novel feature of the present study is the method of visualization of the simulated particle data. Visualization is performed by calculating particle concentrations in the vicinity of each interpolation point used for plotting. The particle concentration at each interpolation point is calculated by summing the number of nearby particles subjected to a Gaussian filter. A standard deviation that scaled with the mesh density was used: a value of half the mean distance

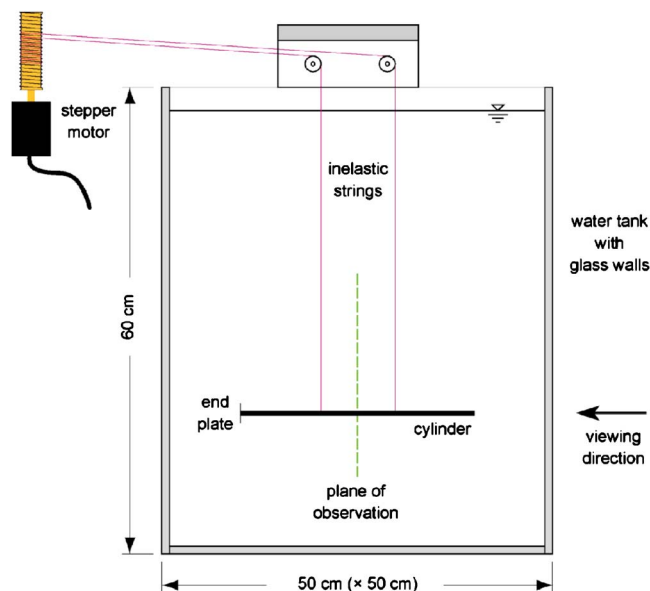


FIG. 3. (Color online) A schematic diagram showing the experimental laser-fluoresced dye-visualization setup. The stepper motor and pulley system permitted carefully controlled vertical motion of the cylinder.

from the node of interest to the three nearest surrounding nodes produced effective results. As integration of a two-dimensional Gaussian function evaluates to unity independent of the size of the variance, this visualization approach produces a constant contour field for a uniform particle concentration. This is true even on meshes with irregular grid spacing, which are common in high-order computational fluid dynamics simulations. The discrete nature of general particle and mesh node distributions mean that the method can introduce moiré patterns, though with sufficiently large particle concentrations these artifacts do not degrade the usefulness of this technique as a visualization tool. The inherent diffusion introduced by the Gaussian profile closely mimics the softness observed in experimental dye visualization, due to both the diffusion of the dye in the water and the dazzling luminescence of concentrated regions of dye. Tests verified that this technique provided images closely matching photographs of laser-fluoresced dyes in water, facilitating the direct comparison between experimentally obtained flows and the computational equivalent computed in this study.

C. Experimental dye visualization

Dye visualization experiments were performed as part of this study, and Fig. 3 shows a schematic diagram of the experimental setup. A circular cylinder with an aspect ratio greater than 20 was suspended from two fine threads in a water tank. The cylinder was first coated in fluorescein dye before subsequently being carefully lowered into the tank to its starting position. The wake was identified by illuminating the dye entraining into the fluid from the cylinder using an argon-ion laser sheet positioned at the midspan of the cylinder.

D. Parameter space

Limited experiments have shown that there is a marked variation in flow states possible when either the Reynolds number or the translation distance (L/D) is varied. Translation distances over the range

$$L/D \geq 1$$

are considered in this investigation. It is well known¹⁵ that above $Re \approx 47$ the wake of a circular cylinder undergoes a transition from a steady two-dimensional wake, comprising a counter-rotating vortex pair attached to the rear of the cylinder, to a periodic wake comprising a street of shed vortices. This transition point affects the possible flow states of the arresting cylinder problem, as above this Reynolds number, symmetry about the wake centerline is broken through a Hopf bifurcation over long translation distances. The simulations in this study do not artificially suppress this instability, and in some cases [when translation distances $L/D \geq O(10)$ were employed], this instability was observed. However, it will later be shown that with translation distances $L/D \leq 5$, the instability was not encountered even up to $Re=1000$. This is consistent with previous experimental observations.¹⁶

A further limitation on the valid parameter space is the transition point for three-dimensionality. For a fully developed wake behind a circular cylinder, this transition occurs at approximately $Re=188.5$,¹⁷ but in this system the three-dimensional transition is not known, as for most L/D ratios the wake and surrounding flow is highly transient and immature in its development. In this study, a Reynolds number range

$$50 \leq Re \leq 1000$$

will be investigated. To determine if the assumption of two-dimensional flow at the higher Reynolds numbers is valid, a Floquet linear stability analysis technique^{9,17} was applied to frozen snapshots of a developing arrested cylinder wake with $L/D=3$ at a range of Reynolds numbers. While flows with $Re \leq 200$ remained two-dimensionally stable, a simulation at $Re=500$ revealed instability of three-dimensional perturbations at times in the vicinity of arrest. At $t^*=0$, wavelengths $\lambda \approx 0.5D$ and $\lambda \geq 8D$ were unstable, and at $t^*=1$, wavelengths $\lambda \geq 4D$ were unstable. Beyond $t^* \geq 2$, stability is restored. A further investigation of these instabilities was not performed in this study, though the short duration over which these three-dimensional modes are unstable means that it is unlikely that three-dimensional transition will be encountered, even at these high Reynolds numbers. It will also be shown that the validating experiments match well with the two-dimensional simulations at Reynolds numbers much higher than the fixed cylinder transition point of the fully developed flow.

E. Grid independence

A detailed grid independence study was performed to examine the temporal and spatial accuracy of the simulations. Arrested cylinder simulations over a range of element orders (N) were performed at a high Reynolds number (Re

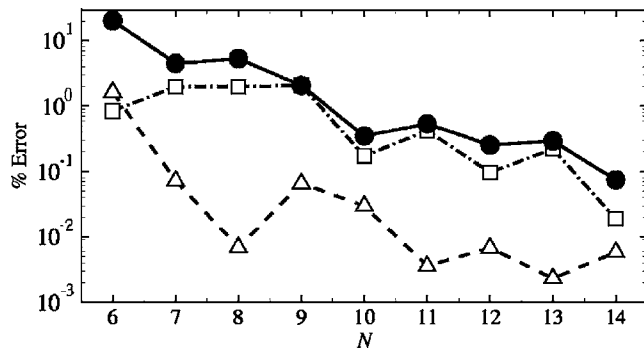


FIG. 4. Drag force error percentages plotted against element order (N), showing convergence of an arrested cylinder simulation with $Re=1000$ and $L/D=3$. Plotted are the percentage errors at $t^*=50$ and 100 (triangles and squares, respectively) and the maximum error for $20 \leq t^* \leq 100$ (solid circles).

=1000) and with a translation distance ($L/D=3$) consistent with those investigated in this study. Drag force time histories were recorded at element orders in the range $6 \leq N \leq 15$, and percentage errors were calculated between each data set and the data with $N=15$. Convergence trends for three percentage errors are plotted in Fig. 4. In this study, simulations were consistently performed with an element order and time step $N=10$, providing an error of less than 0.5% for computations extending 100 time units beyond arrest. The errors are significantly smaller closer to the time of arrest. For instance, the plot demonstrates that the error at $t^*=50$ is better than 0.03%.

III. NUMERICAL VALIDATION

One of the few studies in the past to have tackled an arresting cylinder problem was that of Wang (1989),¹⁸ in which vorticity contour plots and time histories of cylinder drag coefficient were presented. In that work, a numerical study was conducted based on a finite-difference approximation to the vorticity-stream function transport equation. To validate the present spectral-element algorithm and arresting cylinder mesh, simulations were conducted replicating those reported by Wang at $Re=300$, 550, and 1000, with $L/D=2.5$.

The earlier study provided vorticity contour plots at several times, and in Fig. 5 we compare their plots at $t^*=5$ at each Reynolds number with results using the present scheme. The major feature to draw from these comparisons is the excellent match between each pair of near-cylinder vorticity fields. Furthermore, the higher resolution available in the present simulations will permit the flows to be reliably advanced over much longer times.

A quantitative comparison of these results is also possible, as Wang also computed drag coefficient time histories. A comparison between drag coefficients computed in both the present study and that study is provided in Fig. 6. A close similarity is seen between the curves, although in the vicinity of the impulsive changes in motion (at $t=0$ and 2.5), the profiles differ. This discrepancy is also more pronounced at higher Reynolds numbers, and is believed to be caused by an overestimation of surface shear stress in the earlier computations due to the lower-order characteristics of their method.

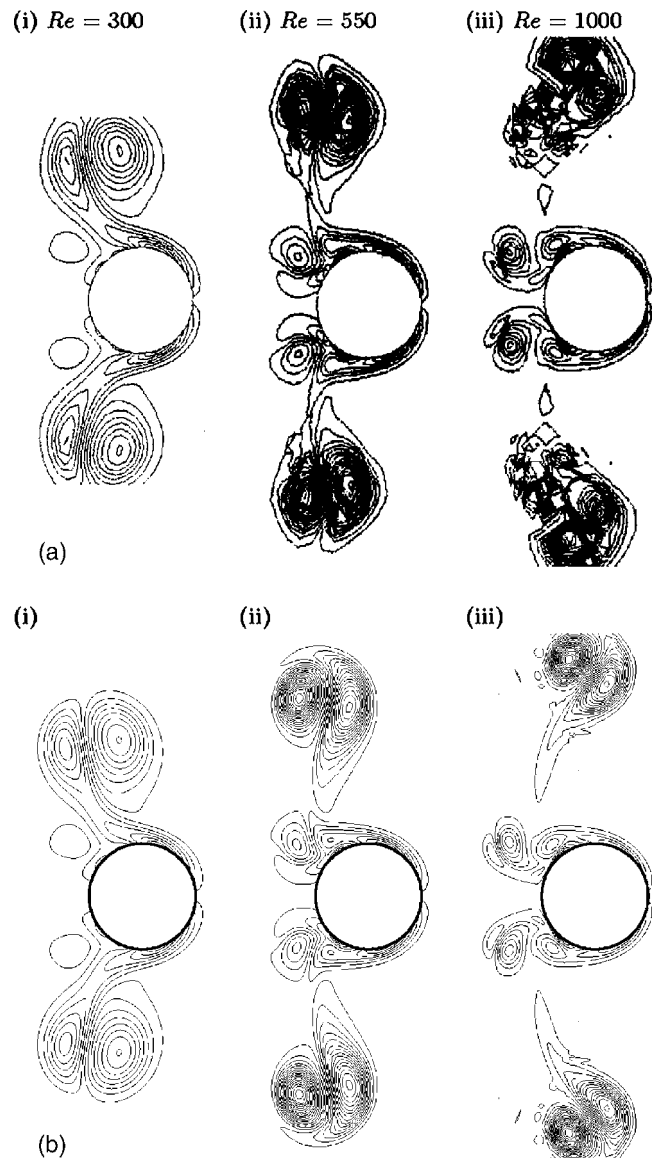


FIG. 5. A comparison between vorticity plots obtained by (a) Ref. 18 and (b) with the present scheme for an arrested cylinder with $L/D=2.5$ at $t^*=5$. Reynolds numbers (i) $Re=300$, (ii) $Re=550$, and (iii) $Re=1000$ are shown. The cylinder was initially moving from right to left, and the same vorticity contour levels are plotted in the two images corresponding to each Reynolds number.

In a subsequent publication, Wang and Dalton⁴ acknowledge that the drag values computed at those times were not meaningful. The curves obtained using the present scheme were found to exhibit virtually no change with variation in time step or element order, indicating that the present results are essentially independent of discretization errors.

Another possible source of discrepancy between experiment and numerical simulation is the time taken to accelerate or decelerate the cylinder to the desired velocity. Numerically, an almost instantaneous (limited by the size of the time step) change in velocity is employed. However, to avoid acceleration discontinuities in the experiments, an S-shaped velocity curve was employed, varying from 0 to U over a distance of $0.01D$, which corresponded to a duration of $0.02D/U$. To verify that differences of this order in startup

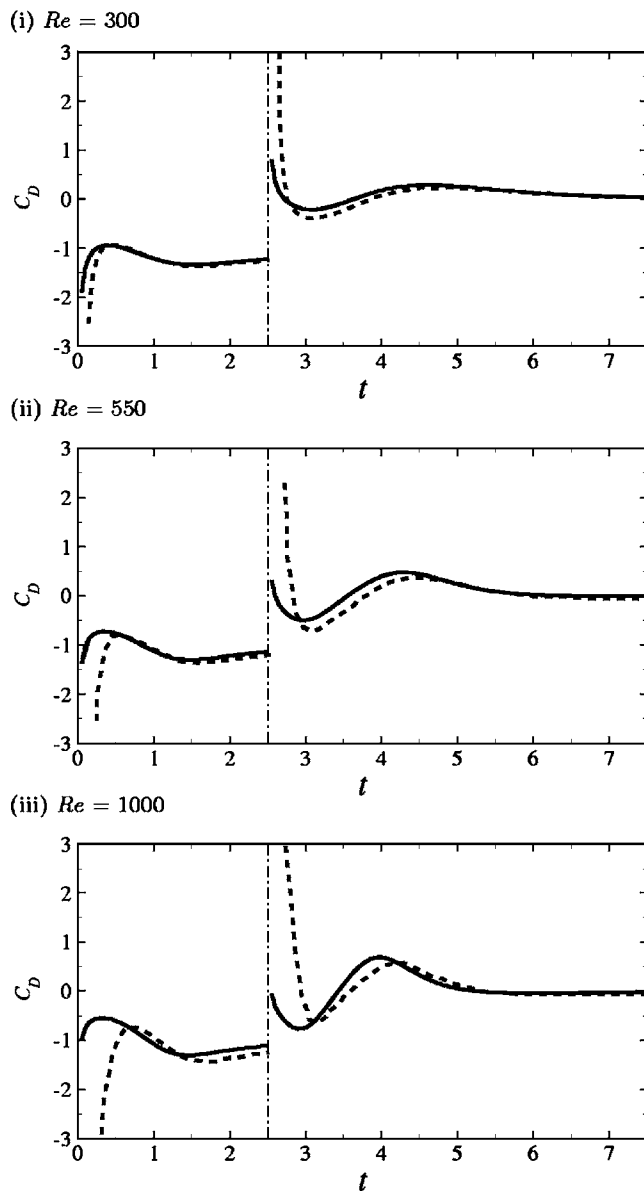


FIG. 6. Drag coefficient (C_D) time histories comparing the computations of Ref. 18 (dotted lines) to the present simulations (solid lines). Arrest is indicated by a dash-dot line at $t=2.5$. Plots show results for (i) $Re=300$, (ii) $Re=550$, and (iii) $Re=1000$.

and arrest time are insignificant, the $Re=1000$ computation with $L/D=2.5$ reported previously was repeated with smoothly varying acceleration and deceleration velocity profiles with durations $0.01D/U$, $0.02D/U$, and $0.05D/U$. When overlaid on the data in Fig. 6(iii), the drag coefficient curves with small but finite arrest times were indistinguishable from the instantaneous-arrest curve. The differences between each curve were also found to rapidly diminish over time; hence these small differences in arrest duration have no impact on the long-time-scale dynamics of an arresting cylinder flow. It can be conclusively stated that the overprediction of drag from Wang¹⁸ is not related to the cylinder arrest time.

Further validation of the present numerical code is provided in the next section, which compares numerical particle

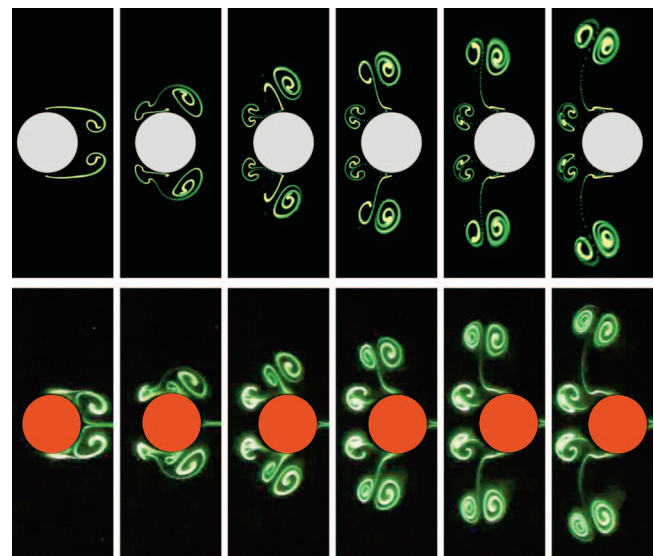


FIG. 7. (Color) Comparison between the computed particle trace simulations (top) and experimental dye visualization (bottom) for an arresting cylinder at $Re=500$ and $L/D=2$. From left to right, nondimensional times $t^*=0, 1, 2, 3, 4, 5$ are shown.

transport and experimental fluorescent dye transport around an arrested cylinder.

IV. RESULTS: COMPARING SIMULATION WITH EXPERIMENT

Figure 7 provides a comparison between an experimentally obtained sequence of images of an arresting cylinder flow and a sequence obtained numerically under the same conditions and at the same nondimensional times. The figure demonstrates high fidelity in the numerical reproduction of vortex structures and kinematics. The excellent agreement with the two-dimensional numerical simulation also verifies that the development of three-dimensional instability is suppressed by the short translation distances in a fashion similar to the delayed onset of wake instability, even for Reynolds numbers far beyond the transition. Here it is seen that over the presented time frame, at a Reynolds number approximately 2.6 times that of the transition Reynolds number for three-dimensionality in circular cylinder wakes, the experimental visualization compares so closely that it is clear that three-dimensional flow features have either not developed, or are insignificant. This verifies the accuracy of the numerical simulations, the validity of the assumption of two-dimensionality, and the suitability of the visualization methods employed in this study, at least for $Re \lesssim 500$.

The previous results were obtained for cases in which the translation distance L/D was too small to permit the cylinder wakes to saturate. When the wake saturates to either a steady or periodic state, it then becomes independent of L/D . Therefore, a translation distance $L/D \rightarrow \infty$ is defined to describe the arrest of cylinders whose wakes have saturated. The results to follow show cylinders at $Re=75$ and 150 that have arrested from a saturated periodic state. A comparison with experimental dye visualization is shown, where the cyl-

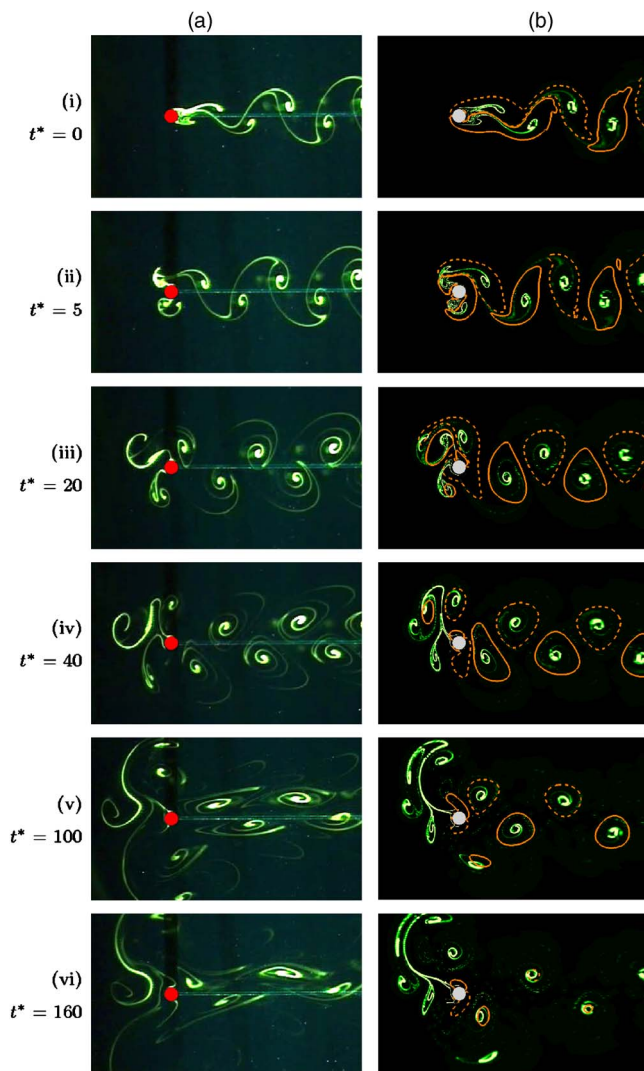


FIG. 8. (Color online) A comparison between (a) an experimental dye visualization with $L/D=67$ and (b) a numerical simulation with $L/D \rightarrow \infty$ at $Re=75$. Contour lines of vorticity (solid and broken lines showing positive and negative vorticity, respectively) are plotted on the numerical frames to elucidate the position of physical vortices in relation to regions of high dye/particle concentration.

inder wake was observed to show vortex shedding consistent with a saturated wake.

For the arrest of a cylinder with a saturated periodic wake at $Re=75$, a comparison between experimental dye-visualization images and corresponding numerical simulation images obtained at the same times is shown in Fig. 8. The experiment was performed with $L/D=67$, sufficient for a fully developed periodic wake to develop. In this figure, a small phase difference exists between arrest points for the experimental and numerical runs, but nevertheless the sequences provide a useful insight into the post-arrest trajectories and dynamics. To assist in comparing the trajectories of actual vortices with the transport of simulated dye, contour lines of vorticity are included in the numerical images. Over long time scales, the dye transport in the experiment is distorted by effects such as thermal buoyancy, which is likely responsible for the smearing of the dye streaks in Fig. 8(a) (v–vi). The figure also demonstrates the need for caution in

equating regions of high dye concentration with high vorticity, as parts (iv–vi) show that the regions of high particle concentration to the left of the cylinder are actually devoid of observable vorticity. Parts (v–vi) demonstrate an impressive phenomenon that occurs as a result of each side of the wake containing a series of like-signed vortices. As these wake vortices convect past the cylinder after arrest, the series of corotating vortices on each side of the cylinder coalesce into a large counter-rotating vortex pair. The cores of these large vortical structures are spaced approximately $6D-7D$ apart, and the pair travels to the left under self-induced propulsion at an estimated speed of $0.02U$.

A similar simulation was conducted at $Re=150$ to establish the Reynolds number dependence of the post-arrest dynamics. The results are shown in Fig. 9 and are very similar to the $Re=75$ case. Possibly the most significant difference is that at $Re=150$, the wake vortices coalesce into larger-scale vortical structures further behind the cylinder than at $Re=75$. For instance, notice how a mushroom-shaped region of dye is cast downstream along the top of the frames [e.g., Fig. 9(b) vi], whereas evidence of a coherent large-scale counter-rotating vortex pair on either side of the cylinder is not apparent.

To quantify the observed differences in long-time-scale flow dynamics around a cylinder arrested from a periodic shedding state at different Reynolds numbers, time histories of the lift and drag on the cylinder after arrest were recorded. Four time histories were recorded at each Reynolds number, with each series corresponding to an arrest at a different phase of the shedding cycle. The results of this analysis are plotted in Fig. 10. After arrest at $Re=75$, the cylinder experiences horizontal forces acting almost exclusively in the direction of cylinder translation. However, at $Re=150$, shortly after arrest the cylinder experiences a force acting in the opposite direction. At long times ($t^* \rightarrow 160$), the forces decrease in magnitude, tending toward the origin. However, even at long times, finite drag coefficients were detected. At $Re=75$, drag coefficients in the range $-0.02 \leq C_D \leq -0.018$ were recorded for all phases at $t^*=160$. For $Re=150$, drag coefficients were recorded over $-0.02 \leq C_D \leq 0$, though the mean value across the four phases was smaller than at $Re=75$. At long times, the small but finite negative drag coefficient at $Re=75$ is induced by the horizontal velocity component generated in the vicinity of the cylinder by the weak counter-rotating super-vortices observed in Fig. 8. The weaker drag coefficients detected at long times at $Re=150$ are consistent with the absence of a coherent large-scale counter-rotating vortex pair in Fig. 9.

V. RESULTS: WAKES AT THE POINT OF ARREST

In Fig. 11, a series of images shows the entrainment of particles into the wake of a cylinder at the point of arrest for $L/D=3$ for a range of Reynolds numbers. With an increase in Reynolds number, a longer thread of particles is observed to spiral into the core of the developing recirculating wake vortices. For each computation, the injection points were fixed at locations $0.05D$ from the cylinder surface at the widest point around the cylinder normal to the direction of mo-

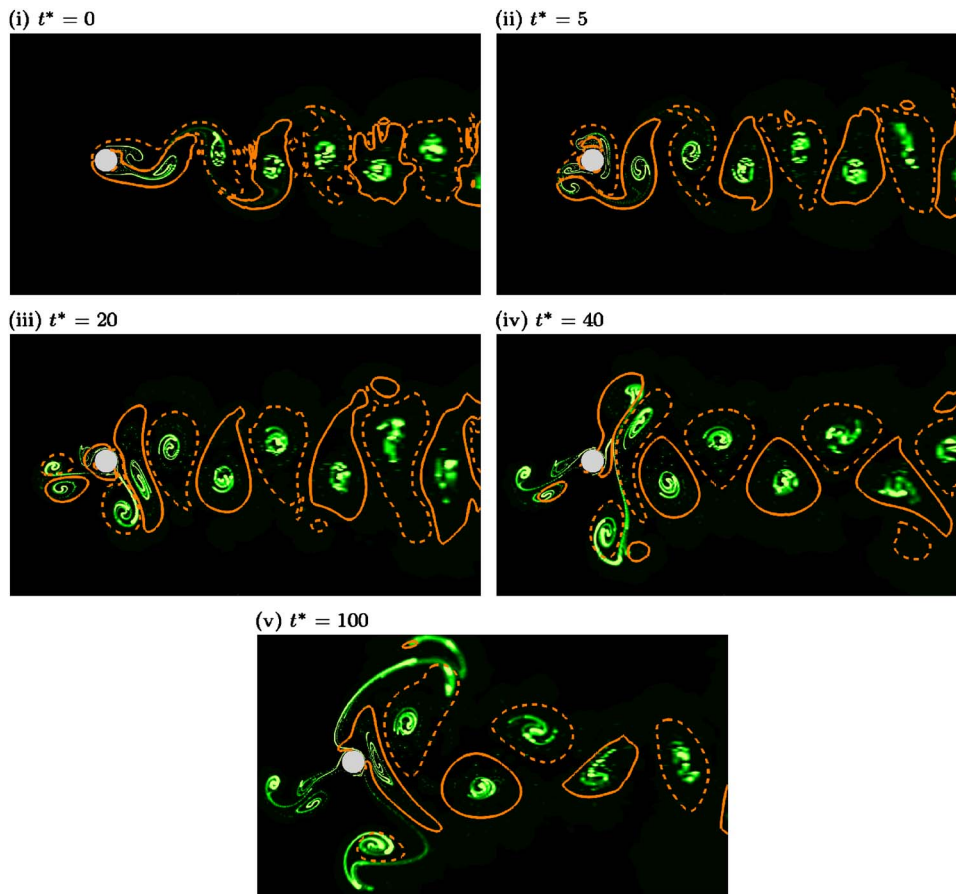


FIG. 9. (Color online) A numerical simulation of a cylinder arrest with $L/D \rightarrow \infty$ at $Re=150$. As with Fig. 8, contour lines of vorticity are plotted on each frame.

tion. Because of this, the speed with which particles entrained into the wake varied with Reynolds number. Due to the reducing thickness of the boundary layer around the cylinder, an increase in Reynolds number caused an increase in the velocity at the injection point, which in turn increased the velocity of the entraining particles, and, hence, the distance the particles traveled over a given amount of time.

It is interesting to also note that despite the majority of these images being captured at Reynolds numbers beyond the nominal transition point for unsteady flow, each of these images retains symmetry about the wake centerline. It should be noted that the instability in the wake behind a free cylinder occurs on the fully formed steady recirculating flow, whereas here the translation length (and hence wake development time) is insufficient for the instability to grow to sufficient amplitude to be visible. Of course, in the numerical simulations the asymmetry leading to shedding has to develop from very low levels (i.e., roundoff error). In the experiments, the background noise is generally orders of magnitude larger and the asymmetry will develop more quickly.

Figure 12 shows a series of images of the wakes at the point of arrest with constant Reynolds number and varying translation distance. This produces a range of wakes that differ significantly at the point of arrest. Here an increase in L/D increases the duration of translation, and hence the wakes are analogous to instantaneous snapshots of the developing wake behind a circular cylinder. A Reynolds number of $Re=100$ was chosen to reveal any deviation from symmetry due to the development of instability in the cylinder

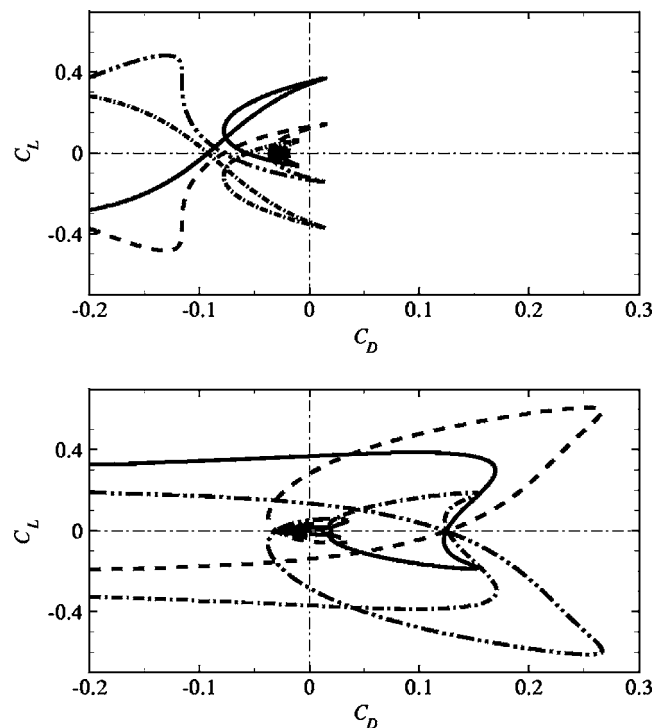


FIG. 10. Plots of C_L against C_D computed over $0 \leq t^* \leq 160$ at (top) $Re=75$ and (bottom) $Re=150$. In each plot, the cylinder was arrested from a periodic shedding state, and the four trends were captured by arresting the cylinder at four equispaced phases over the shedding cycle. Lines of zero lift and drag are added for guidance. At arrest, a high negative drag is experienced, and as time progresses, the trends meander toward the origin.

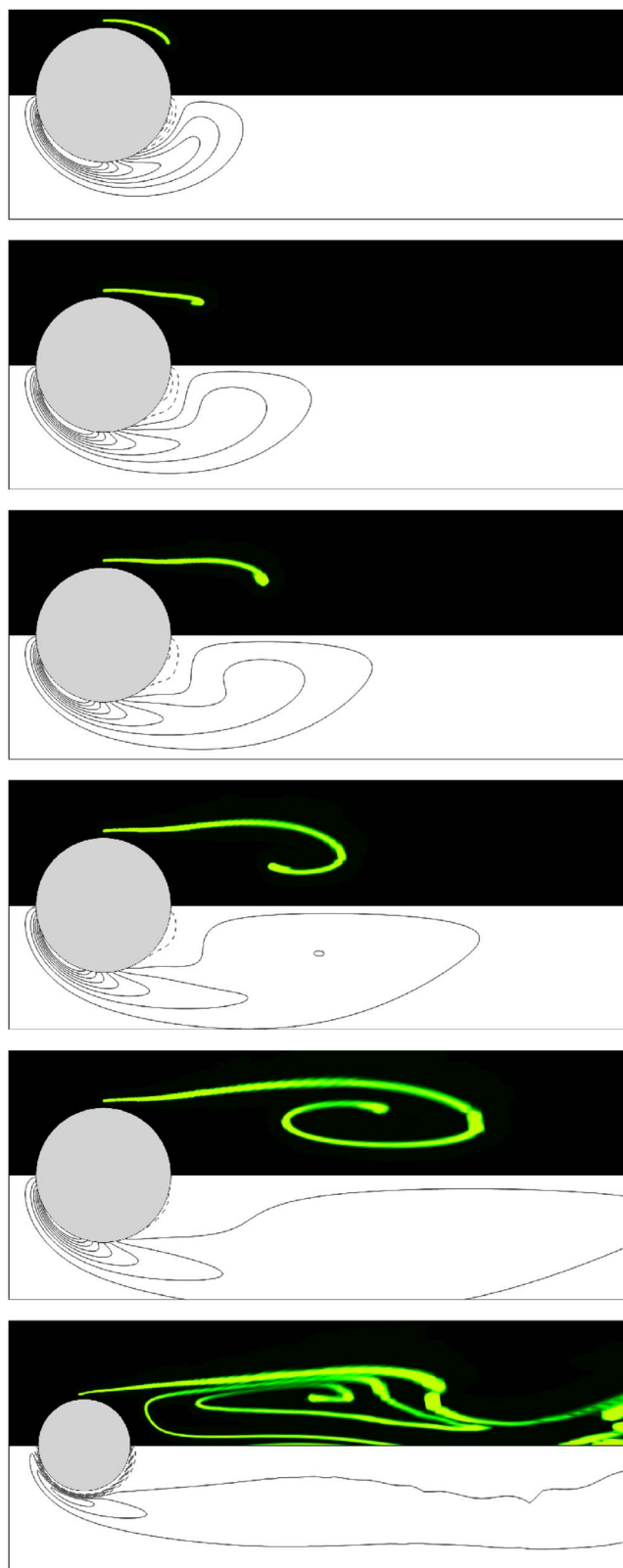
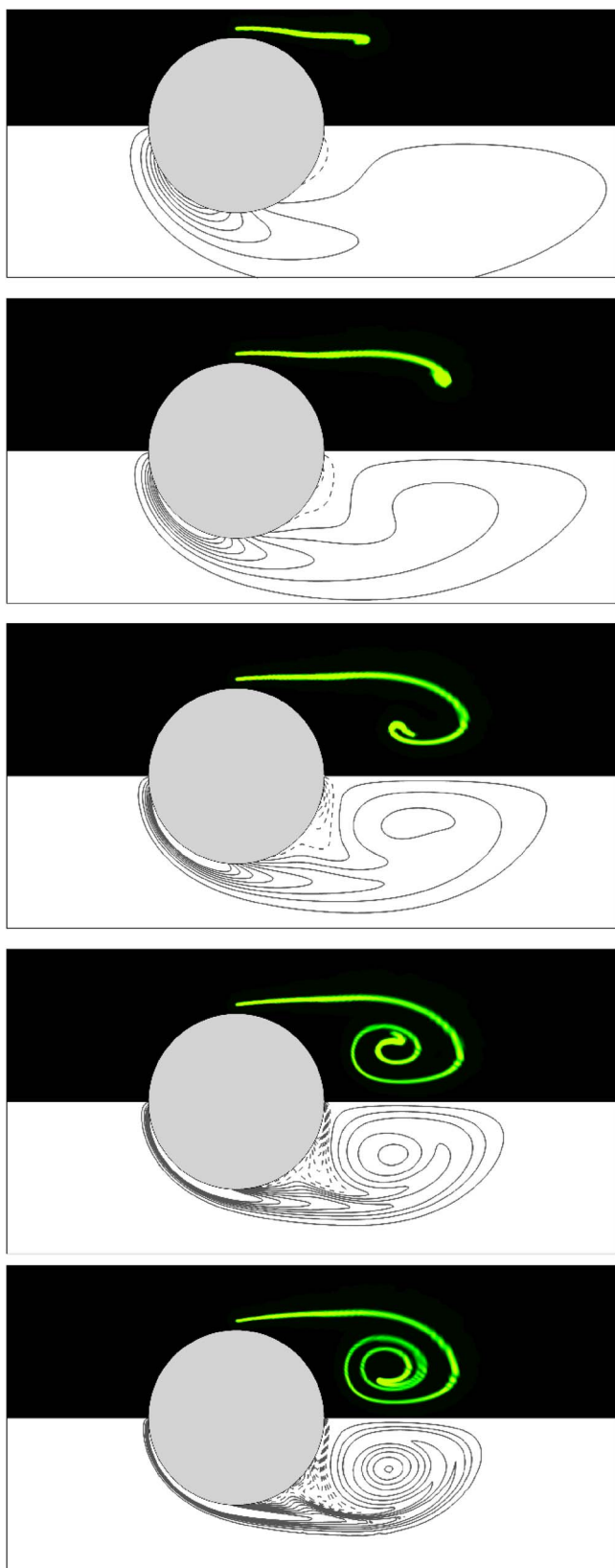


FIG. 11. (Color online) Cylinder wakes at the point of arrest after a translation of $L/D=3$, at Reynolds numbers (top to bottom) $Re=50, 100, 200, 500,$ and 1000 . Simulated-particle concentration is plotted on the upper half of each frame (particles are injected at the widest point of the cylinder). Vorticity contours are plotted on the lower half of each frame, with 16 contour levels equispaced between $\omega_z \pm 15.0$, and dashed lines showing negative values. Prior to arrest, the cylinder was moving from right to left.

FIG. 12. (Color online) Wakes at the point of arrest with $Re=100$ and translation distance (top to bottom) of $L/D=1, 2, 3, 5, 10,$ and 60 . Contour levels, shading, and cylinder orientation are as per Fig. 11.

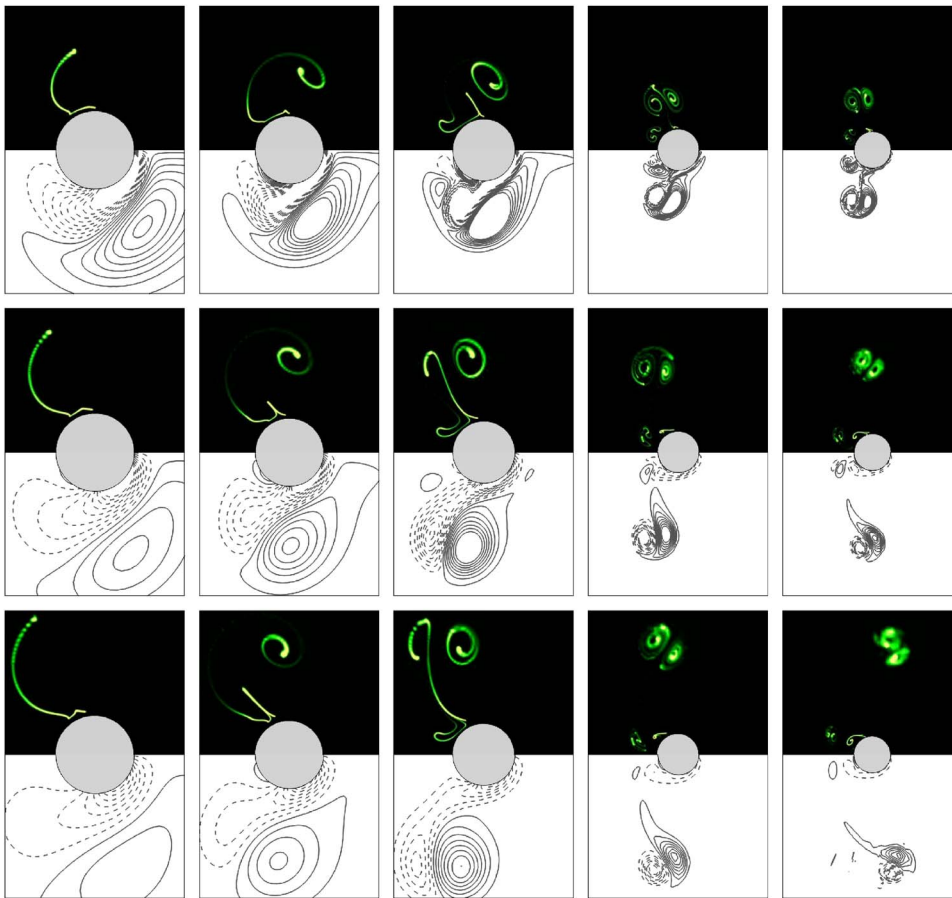


FIG. 13. (Color online) The flow past an arrested cylinder with $L/D=3$ plotted at times (top) $t^*=3$, (middle) 6, and (bottom) 9 after arrest, respectively. From left to right, Reynolds numbers $Re=50, 100, 200, 500$, and 1000 are shown. Prior to arrest, the cylinders were moving from right to left. The upper half of each frame shows particle concentration, and the lower half shows vorticity contour lines. Negative vorticity is indicated by dashed lines, and for each Reynolds number the vorticity contours range between the minimum and maximum vorticity recorded at $t^*=9$.

wake. For shorter translation distances ($L/D \leq 10$), the wake remains symmetrical about the wake centerline, but for $L/D=60$, the wake exhibits the early stages of the development of a Kármán vortex street, with broken wake centerline symmetry.

VI. RESULTS: VORTEX DYNAMICS IN THE STATIONARY PHASE

Following the arrest of the cylinder motion, the developing wake vortices are carried toward and around the circular cylinder by the momentum in the surrounding fluid. Past studies^{5,6} have shown that for an arresting sphere, this backflow of the wake vortices causes induced counter-rotating vortices to develop at the surface of the body, pairing with each passing wake vortex. The present computations reveal a rich variety of vortex dynamics in the surrounding fluid for arresting circular cylinders with variation in both Reynolds number and translation distance.

At lower Reynolds numbers, the strong viscous diffusion causes a very rapid decay of the residual motion toward a motionless state. The images in Fig. 13 demonstrate the effect of Reynolds number changes on the flow patterns at several times following arrest for cylinders with translation distance $L/D=3$.

Several striking observations can be made about the vortex dynamics illustrated by the flows in Fig. 13. First, notice that with an increase in Reynolds number, the simulated dye is drawn greater distances from the cylinder. It is apparent,

especially from the simulations at Reynolds numbers $Re=200$ and above, that the backwash of the wake vortices over the cylinder induces a secondary counter-rotating vortex of a similar but not equal magnitude. These primary and secondary vortices pair up and self-propel away from the cylinder. Due to the circulation difference between the primary and secondary vortices in each pair, the trajectory of the pair is curved, and in each case this curvature deviates away from the original direction of cylinder motion. The speed of this vortex-pair convection increases with Reynolds number, increasing the distance traveled. At higher Reynolds numbers, the formation of the secondary vortices leads to the formation of smaller vortex features near the upstream surface of the cylinder. Figure 14 provides a detailed view of the evo-

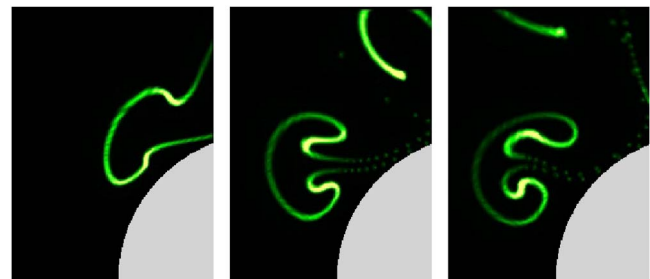


FIG. 14. (Color online) Detailed view of the upstream surface of the cylinder at times (left to right) $t^*=1, 2$, and 3 after arrest, with constant $L/D=3$, at Reynolds numbers $Re=500$. Prior to arrest, the cylinder was moving from right to left.

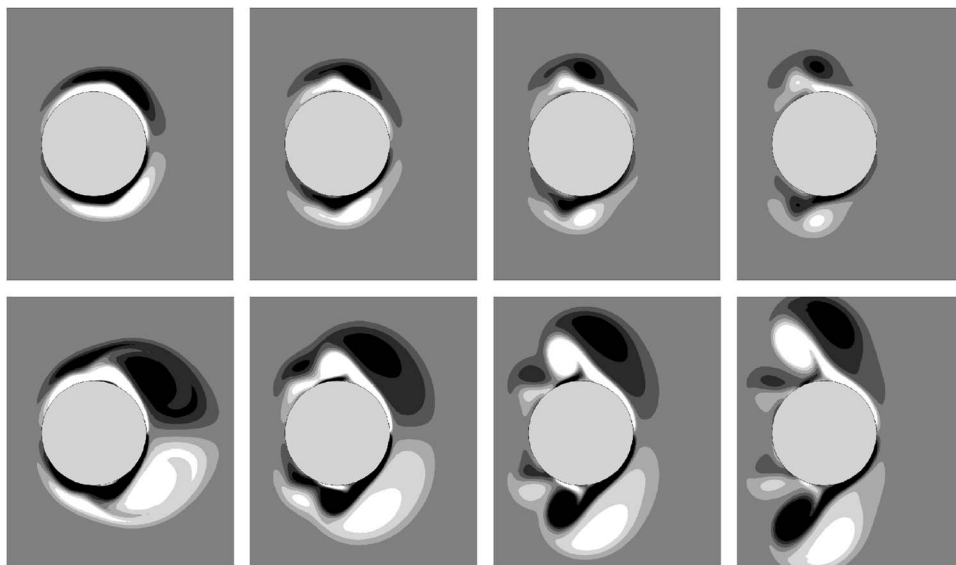


FIG. 15. A contour plot of vorticity around arresting cylinders with (top) $L/D=1$ and (bottom) $L/D=3$. Times $t^*=0.5, 1.0, 1.5,$ and 2 are shown from left to right. Prior to arrest, the cylinder was moving right to left, and light and dark contours represent regions of positive and negative vorticity, respectively. Six equispaced nondimensional vorticity contour levels are plotted over the range $-5.0 \leq \omega_z \leq 5.0$ in each frame.

lution of these structures at $Re=500$ over a short duration.

The small vortex structures shown in Fig. 14 are counter-rotating pair vortices, which appear to develop as a result of the injection of narrow jets of fluid from over the downstream surfaces of the cylinder, likely a by-product of the formation of the strong secondary vortices pairing with the wake vortices. The role these vortices play in promoting the outward propulsion of the main vortex pairs will now be explored.

For short translation distances (e.g., $L/D \approx 1$), the wake vortices do not divert outwards as they pass over the arrested cylinder; instead, they tend to continue their forward propulsion. At long times, they form a large counter-rotating vortex pair that gradually dissipates at a location beyond the final position of the cylinder. The final position of these vortices was found to be dependent on Reynolds number, with higher Reynolds numbers permitting the vortices to travel further from the cylinder, but over a Reynolds number range $200 \leq Re \leq 1000$, the final vortex core positions ranged approximately $1D-4D$ from the center of the cylinder.

In order to investigate this phenomenon further, sequences of contour plots of vorticity for arresting cylinders at $Re=500$ are shown in Fig. 15. The translation distances of the two sequences are $L/D=1$ and 3 , which represent cases in which wake vortices continue past the cylinder after arrest, or propel away from the cylinder in a transverse direction, respectively. Just after the point of arrest, the reversed flow over the cylinder creates regions of opposite-sign vorticity at the cylinder surface. It is this opposite-sign vorticity that is drawn into a counter-rotating vortex that pairs with each wake vortex. In the $L/D=1$ sequence, the distribution of vorticity created during the cylinder motion (the outer bands of vorticity) and the induced opposite-sign vorticity (the inner bands of vorticity) are similar, enveloping each side of the cylinder in a nearly symmetrical fashion with respect to the direction of cylinder motion. Not surprisingly, an exception is a noticeable skewing of the cylinder motion-induced vorticity strength over the aft of the cylinder due to the small wake formation during translation. The $L/D=3$ sequence is

markedly different, with the initial frame showing that wake vortices with diameters approximately $0.6D$ have developed behind the cylinder.

Over time, the opposite-sign vorticity bands in the $L/D=1$ sequence are seen to be drawn into a single counter-rotating vortex pair, which is then free to convect beyond the cylinder in the direction of the original cylinder motion. In contrast, for $L/D=3$, the opposite-sign vorticity bands around the cylinder are shown to split into two distinct counter-rotating vortex pairs on each side of the cylinder. These include a pair of large vortices comprising the wake vortex and the main induced vortex, and a substantially smaller secondary pair that develops from boundary layer vorticity at the front of the cylinder. During its motion, and after arrest, vorticity of both signs feeds the smaller vortex pair. The strength of the wake vortex induces a strong pair vortex, which in turn draws fluid toward the surface of the cylinder immediately upstream of the main vortex pair. This fluid entrainment then causes the vorticity bands to split into the primary and secondary vortex pairs, which can be seen to develop through the time sequence shown.

A focus of this paper is the vortex dynamics over longer times than shown by the sequence in Fig. 15. A particularly interesting case arose for an arresting cylinder with $L/D=3$ at $Re=1000$, which is shown in Fig. 16. It can be seen that over long times, the primary pairs of wake and induced vortices self-propelled in graceful arcs away from the cylinder and toward the downstream direction. An unequal circulation in these vortex pairs caused the curved trajectories, and it is striking to observe that at $t^* \approx 35$, the vortex pairs on each side of the wake collided at the midplane approximately $4D$ behind the cylinder. This collision resulted in pairing of both the two wake and two induced vortices, which then propelled away from each other along the wake centerline. For the vortex pair that originated as the wake vortices, this final propulsion caused them to again impact the rear of the cylinder, before convecting outwards. The encounter between the two main vortex pairs behind the cylinder resembles the

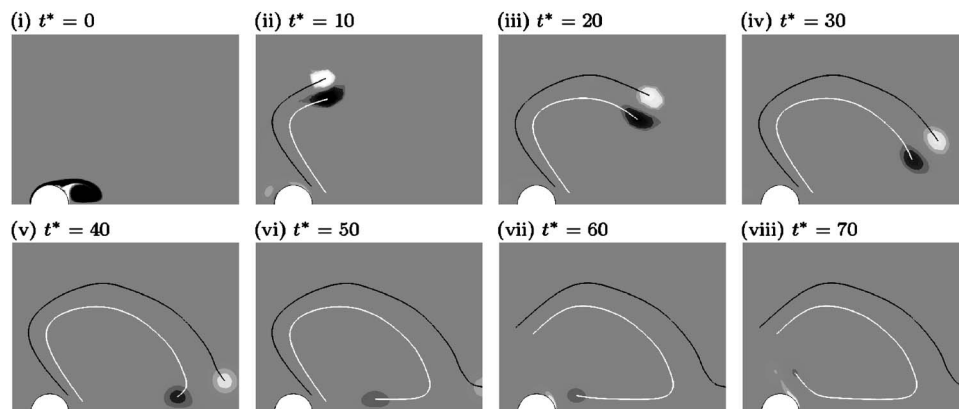


FIG. 16. A time sequence of vorticity around an arrested cylinder with $L/D = 3$ and $Re = 1000$ at different times after arrest. Cylinder orientation and contour shading are as per Fig. 15, and six equispaced nondimensional vorticity contour levels are plotted over the range $-3.0 \leq \omega_z \leq 3.0$ in each frame. The trajectories of the induced and wake vortices are indicated by black and white lines, respectively.

interaction of a vortex pair with a solid wall (i.e., ground effect with image vortices).

VII. RESULTS: VORTEX TRAJECTORIES IN THE STATIONARY PHASE

The plot in Fig. 17 shows the loci of the cores of both the primary wake vortex and the secondary induced vortex over times $0 \leq t^* \leq 24$ for a range of Reynolds numbers when a constant translation distance $L/D = 3$ was employed. The vortex location was taken to be the point of maximum vorticity magnitude within a region of closed vorticity isocontours. This plot is revealing as it corroborates observations discerned from the simulated particle tracking images presented in this study.

Due to the significant diffusion in the flow at $Re = 50$, no secondary induced vortex was formed. The region of opposite-sign vorticity associated with the backwash boundary layer remained attached to the surface of the cylinder. In this simulation, the wake vortex convected almost normal to the original direction of cylinder motion at a slower pace than in the higher-Reynolds-number simulations. In each of the cases from $Re = 100$ to 1000 , a secondary induced vortex was detected, although at $Re = 100$ this vortex was only observed for $6 \leq t^* \leq 18$. At lower Reynolds numbers, the secondary vortex was found to be weaker, and as the vortex pair convected away from the cylinder, they diffused more rapidly than in the higher-Reynolds-number cases. This resulted in a slower migration and shorter trajectories at lower Reynolds numbers than at the higher Reynolds numbers. A curious phenomenon was observed at higher Reynolds numbers, where the longer trajectories traced by the vortices were seen to curve outwards and backwards, eventually traveling in the direction opposite to the original direction of travel of the cylinder and the wake. At the highest Reynolds number investigated ($Re = 1000$), this effect was so pronounced that the vortices began to migrate back toward the wake centerline. In every case displayed in the plot in Fig. 17, symmetry about the wake centerline was observed. This implies that with sufficiently short cylinder translations, the Hopf bifurcation of the wake is not given sufficient time to evolve, even with computations at Reynolds numbers 20 times the critical Reynolds number. However, the final image in Fig. 12 does demonstrate that given sufficiently long translation times, asymmetry will eventually develop in these flows.

Vortex core trajectories at a constant Reynolds number ($Re = 100$) are shown in Fig. 18 for a range of translation distances $1 \leq L/D \leq 10$. This plot demonstrates that at this Reynolds number, there is only a weak dependence of the vortex core trajectories on L/D . Notice that especially for the wake vortices, the final path taken was almost independent of translation distance despite the markedly different start locations of each trajectory. The secondary induced vortices tended to be substantially weaker; only emerging at six time units after arrest for $L/D = 3, 5, \text{ and } 10$, and not being observed at all at lower translation distances.

A more interesting variation in trajectory is found with varying translation distance at higher Reynolds numbers. Figure 19 shows primary vortex pair trajectories at $Re = 500$ for $L/D = 1, 3, \text{ and } 5$. At $L/D = 1$, the induced vortex is weak and is quickly consumed by the larger wake vortex and additional negative-sign vorticity in the vicinity of the forward side of the cylinder. The wake vortex is then free to convect on the wake backwash over the cylinder, where it maintains a further slow propulsion in the upstream direction by pairing with the opposite-sign wake vortex on the other side of the cylinder. At $L/D = 3$, a highly curved trajectory is found, with the vortex pair migrating approximately $3D$ away from the cylinder in the transverse direction, before turning toward the wake centerline. At times $t^* \gtrsim 60$, the wake vortex is seen to deviate away from the induced vortex in a direction toward the rear of the cylinder. The radius of curvature of the path taken by the vortex pair is approximately $1.4D$. At $L/D = 5$, a larger radius of curvature of the trajectories is observed, with the vortex pair path exhibiting a radius of curvature increase from approximately $2.2D$ to $4D$ over times $t^* \approx 5$ to 75 .

The trajectory curvature differences at $Re = 500$ between $L/D = 3$ and 5 are supported by predictions of the path curvature from theory. The ratio of circulation between the wake vortex and the induced vortex (Γ_w and Γ_i , respectively) was computed, as was the distance between the vortex cores (b). Plots of the variation in these parameters are shown in Fig. 20(i-ii). The Biot-Savart law can be used to show that the radius of curvature of the trajectory of a pair of point vortices with circulations Γ_1 and Γ_2 , separated by a distance b , is given by

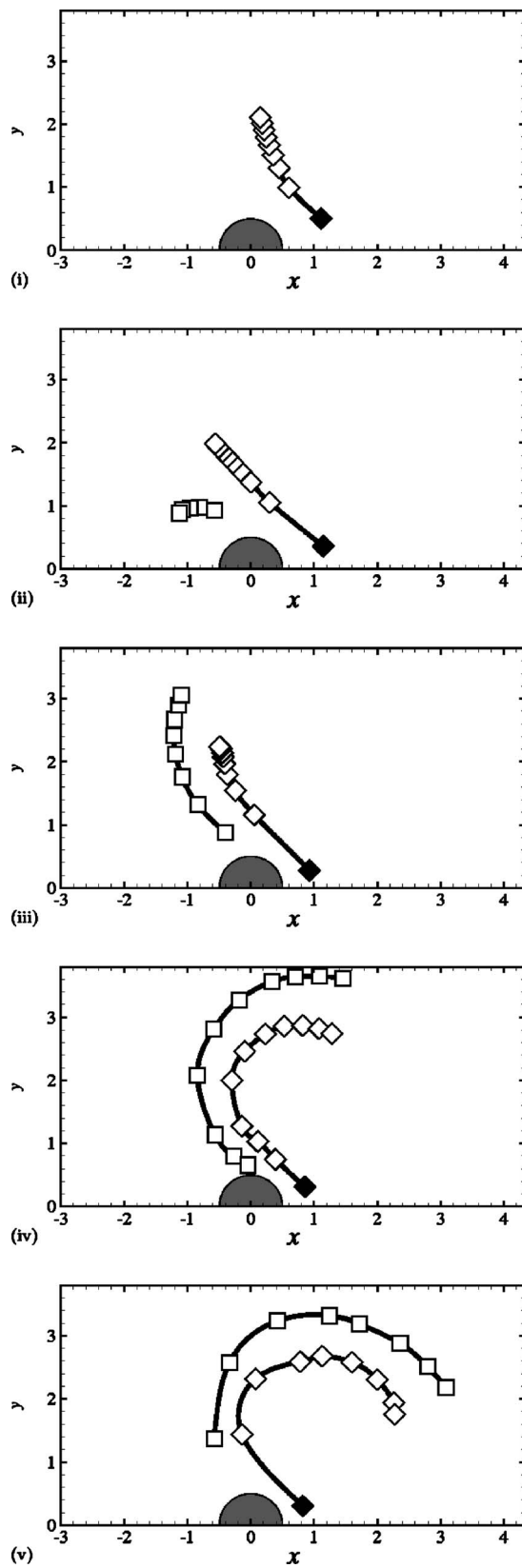


FIG. 17. Loci of the cores of the primary wake vortex (\diamond) and the secondary induced vortex (\square) from time $t^*=0$ (solid symbols) through to $t^*=24$ (open symbols). A constant $L/D=3$ was used, and Reynolds numbers (i) $Re=50$, (ii) 100, (iii) 200, (iv) 500, and (v) 1000 are displayed. The cylinder is shown in gray. Due to symmetry in the flow, only the trajectories in one-half of the wake are shown.

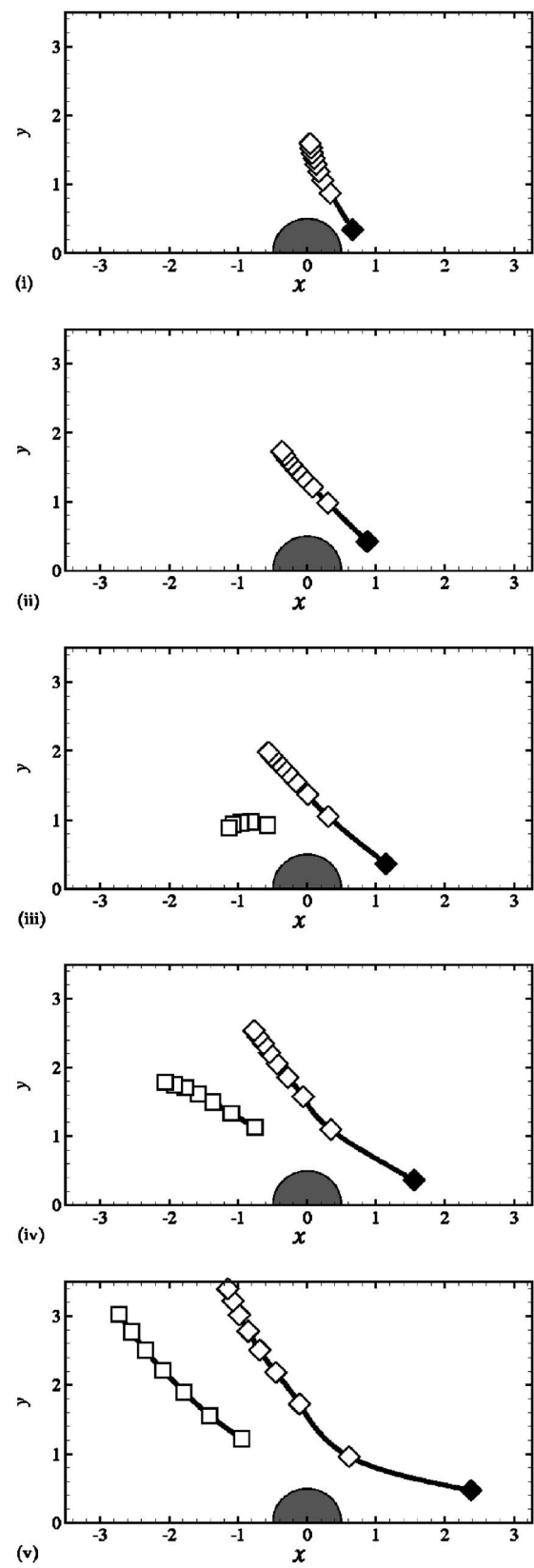


FIG. 18. Loci of the cores of the primary wake vortex and the secondary induced vortex from time $t^*=0$ through to $t^*=24$ for simulations at $Re = 100$ at (i) $L/D=1$, (ii) 2, (iii) 3, (iv) 5, and (v) 10. Symbols and orientation are as in Fig. 17.

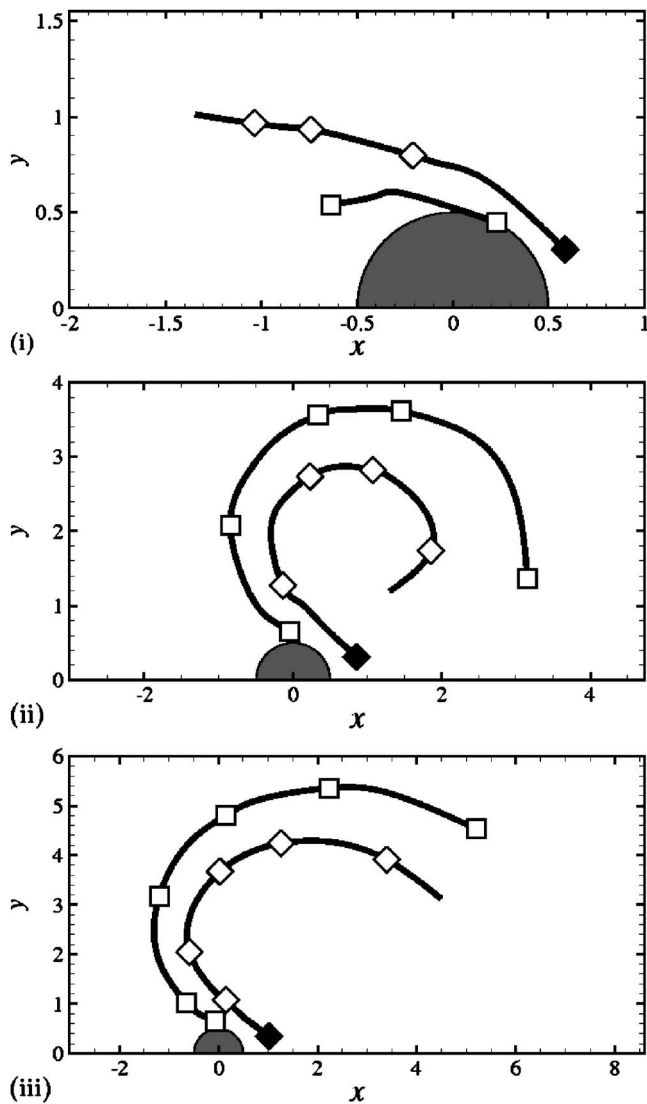


FIG. 19. Loci of the cores of the primary wake vortex and the secondary induced vortex from time $t^*=0$ through to $t^*=75$ for simulations at $Re=500$ at (i) $L/D=1$, (ii) 3, and (iii) 5. Symbols and orientation are as in Fig. 17.

$$R = \left| \frac{b}{2} \left(\frac{1 - \Gamma_1/\Gamma_2}{1 + \Gamma_1/\Gamma_2} \right) \right|. \tag{1}$$

Therefore, a greater difference between vortex circulations or a smaller distance between the vortices can both act to decrease the radius of curvature of their trajectory. When comparing against the $L/D=5$ result, Fig. 20 (i-ii) shows that the $L/D=3$ case exhibits smaller vortex spacing (up to $t^* \approx 30$) and a larger circulation ratio magnitude over the plotted range of t^* . In Fig. 20 (iii), the radius of curvature calculated from theory for the present cases at $Re=500$ is plotted. Despite a number of factors impeding a quantitative comparison between the predicted curvature trend and the curvatures measured from the trajectory plots (including the difference between an ideal point vortex in an inviscid fluid and the computed vortices in a viscous fluid, and the modification of trajectory paths by residual bulk flows from the wake backwash over the arresting cylinder), a reasonable quantitative agreement was found when comparing predicted and mea-

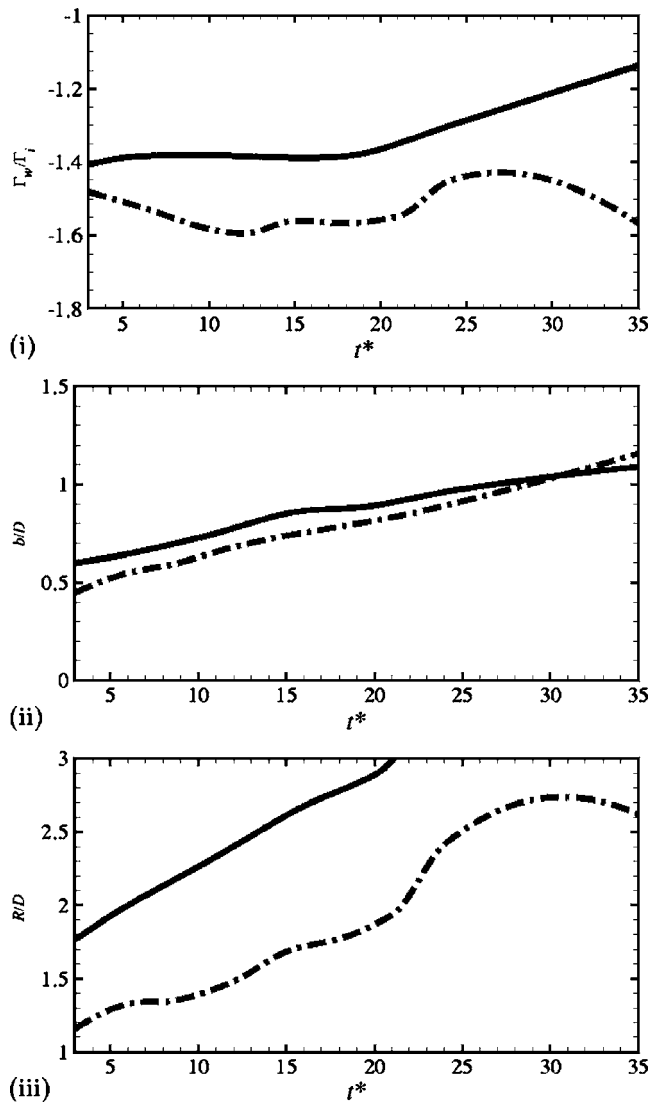


FIG. 20. (i) Ratio of wake to induced vortex circulation (Γ_w/Γ_i) plotted against t^* for a cylinder with $Re=500$ and $L/D=3$ (dashed line) and 5 (solid line). (ii) Dimensionless vortex spacing (b/D) plotted against t^* for the same cases as (i). (iii) Dimensionless theoretical radius of curvature (R/D) derived from Eq. (1) plotted against t^* for the same cases as (i).

sured trajectory curvatures. The ratio of the path curvatures, measured from the trajectory plots for the cases $L/D=5$ to $L/D=3$, is $R_5/R_3 \approx 2.2D/1.4D \approx 1.6$. The predicted curvatures in Fig. 20 (iii) reveal that over the range $3 \leq t^* \leq 25$, the ratio of predicted radii of curvature ranged between 1.51 and 1.63, in excellent agreement with the measured value of 1.6. Furthermore, the predicted R/D trends agree well with the trajectory plots in Fig. 19 (ii-iii). Over times $5 \leq t^* \leq 15$, the difference between the predicted R/D values and the estimated values taken from the trajectory plots is within approximately 10%. An increase in curvature radius is also observed with an increase in t^* . This increase is reflected in the trajectory plots, which exhibit an outwardly spiraling curved path.

VIII. CONCLUSIONS

A range of translation distances and Reynolds numbers has been investigated for an arresting cylinder. A novel technique for visualization of the computed flows was employed

whereby simulated particle tracking was used to mimic the entrainment of dye into the wake in experimental dye visualization. Plots of the concentration of particles based on a Gaussian weighted distribution local to each interpolation point very closely matched the experimental photography. This technique provides a useful tool for validation of numerical results against existing experimental dye visualizations.

Time histories of drag and lift coefficients recorded over long time scales following arrest of a cylinder from a periodic shedding state revealed, for $Re=75$, that the wake vortices rolled up into a massive counter-rotating vortex pair with a core spacing in the order of seven cylinder diameters. Even at post-arrest times $t^* \gtrsim O(100)$, this vortex pair induces a detectable drag force on the cylinder, acting in the original direction of translation. At $Re=150$, this effect was less pronounced, as the wake vortices failed to coalesce so successfully.

Comparisons showed that the limited available arresting cylinder studies in the literature exhibited a close agreement with the present study. For the first time, detailed trajectory paths have been established up to $t^*=75$, for both the wake and induced vortices, for Reynolds numbers $50 \leq Re \leq 1000$ and translation distances $1 \leq L/D \leq 10$.

These simulations have revealed that with a translation distance $L/D=3$, the vortices around the cylinder tend to deviate sideways and backwards rather than rolling past the cylinder and continuing in the direction of original cylinder motion. The viscous effects at lower Reynolds numbers were observed to retard the propagation of the counter-rotating vortex pairs, and at higher Reynolds numbers the vortices traveled larger distances, in some cases (e.g., $Re=1000$) turning back on themselves and colliding again behind the cylinder. For longer translation distances, wake instability eventually destroyed the symmetry about the wake centerline for Reynolds numbers above the transition point.

At the point of arrest, both the size of the wake recirculation bubble and the strength of the wake vortices were observed to increase with either Reynolds number or translation difference.

Predictions of the curvature for wake and induced vortex pair trajectories based on computed vortex circulations were in good agreement with curvatures measured directly from trajectory plots at $Re=500$ and a range of translation distances. A translation distance of $L/D=3$ resulted in a tightly curved path, whereas at $L/D=5$ a path with a radius of curvature approximately 1.5 times greater was observed.

It was observed experimentally that the computed and observed vortex trajectories began to deviate after approximately 10 time units. It is believed that this is due to the evolution of small asymmetries and thermal effects in the

experiments, though the evolution of three-dimensional instability cannot be discounted. This would be a useful avenue for investigation in a future study.

ACKNOWLEDGMENTS

We thank Dr. Xuegeng Wang and Professor Charles Dalton for granting permission to reproduce Fig. 5(a) from Ref. 18. This work was supported by the Australian Research Council through ARC Discovery Grants Nos. DP0555897 and DP0665736. Numerical computations were conducted using the resources of the Australian Partnership for Advanced Computing (APAC) National Facility, through the Merit Allocation Scheme.

- ¹M. Braza, P. Chassing, and H. Ha Minh, "Numerical study and physical analysis of the pressure and velocity fields in the near wake of a circular cylinder," *J. Fluid Mech.* **165**, 79 (1986).
- ²P. Koumoutsakis and A. Leonard, "High-resolution simulations of the flow around an impulsively started cylinder using vortex method," *J. Fluid Mech.* **296**, 1 (1995).
- ³M. Tatsuno and S. Taneda, "Visualization of the unsteady flow past cylinders and plates decelerated from a steady speed," *J. Phys. Soc. Jpn.* **31**, 1266 (1971).
- ⁴W. Wang and C. Dalton, "Numerical solutions for impulsively started and decelerated viscous flow past a circular cylinder," *Int. J. Numer. Methods Fluids* **12**, 383 (1991).
- ⁵T. Leweke, M. C. Thompson, and K. Hourigan, "Vortex dynamics associated with the collision of a sphere with a wall," *Phys. Fluids* **16**, L74 (2004).
- ⁶M. C. Thompson, T. Leweke, and K. Hourigan, "Sphere-wall collision: Vortex dynamics and stability," *J. Fluid Mech.* **575**, 121 (2007).
- ⁷G. E. Karniadakis and S. J. Sherwin, *Spectral/hp Element Methods for Computational Fluid Dynamics* (Oxford University Press, Oxford, 2005).
- ⁸M. C. Thompson, K. Hourigan, and J. Sheridan, "Three-dimensional instabilities in the wake of a circular cylinder," *Exp. Therm. Fluid Sci.* **12**, 190 (1996).
- ⁹G. J. Sheard, M. C. Thompson, and K. Hourigan, "From spheres to circular cylinders: The stability and flow structures of bluff ring wakes," *J. Fluid Mech.* **492**, 147 (2003).
- ¹⁰G. J. Sheard, M. C. Thompson, K. Hourigan, and T. Leweke, "The evolution of a subharmonic mode in a vortex street," *J. Fluid Mech.* **534**, 23 (2005).
- ¹¹H. M. Blackburn and S. J. Sherwin, "Formulation of a Galerkin spectral element-Fourier method for three-dimensional incompressible flow in cylindrical geometries," *J. Comput. Phys.* **197**, 759 (2004).
- ¹²G. E. Karniadakis, M. Israeli, and S. A. Orszag, "High-order splitting methods for the incompressible Navier-Stokes equations," *J. Comput. Phys.* **97**, 414 (1991).
- ¹³C. H. K. Williamson, "Defining a universal and continuous Strouhal-Reynolds number relationship for the laminar vortex shedding of a circular cylinder," *Phys. Fluids* **31**, 2742 (1988).
- ¹⁴G. Coppola, S. J. Sherwin, and J. Peiró, "Non-linear particle tracking for high-order elements," *J. Comput. Phys.* **172**, 356 (2001).
- ¹⁵M. Provansal, C. Mathis, and L. Boyer, "Bénard-von Kármán instability: Transient and forced regimes," *J. Fluid Mech.* **182**, 1 (1987).
- ¹⁶H. Honji and S. Taneda, "Unsteady flow past a circular cylinder," *J. Phys. Soc. Jpn.* **27**, 1668 (1969).
- ¹⁷D. Barkley and R. D. Henderson, "Three-dimensional Floquet stability analysis of the wake of a circular cylinder," *J. Fluid Mech.* **322**, 215 (1996).
- ¹⁸X. Wang, Ph.D. thesis, University of Houston (1989).